Diagnosing ENSO and Global Warming Tropical Precipitation Shifts Using Surface Relative Humidity and Temperature

Alexander Todd, Matthew Collins, and F. Hugo Lambert

University of Exeter, Exeter, United Kingdom

Robin Chadwick

Met Office Hadley Centre, Exeter, United Kingdom

ABSTRACT

Large uncertainty remains in future projections of tropical precipitation change under global warming. A simplified method for diagnosing tropical precipitation change is tested here on present-day El Niño–Southern Oscillation (ENSO) precipitation shifts. This method, based on the weak temperature gradient approximation, assumes precipitation is associated with local surface relative humidity (RH) and surface air temperature (SAT), relative to the tropical mean. Observed and simulated changes in RH and SAT are subsequently used to diagnose changes in precipitation. Present-day ENSO precipitation shifts are successfully diagnosed using observations (correlation $r = 0.69$) and an ensemble of atmosphere-only ($0.51 \leq r \leq 0.8$) and coupled ($0.5 \leq r \leq 0.87$) climate model simulations. RH ($r = 0.56$) is much more influential than SAT ($r = 0.27$) in determining ENSO precipitation shifts for observations and climate model simulations over both land and ocean. Using intermodel differences, a significant relationship is demonstrated between method performance over ocean for present-day ENSO and projected global warming ($r = 0.68$). As a caveat, the authors note that mechanisms leading to ENSO-related precipitation changes are not a direct analog for global warming–related precipitation changes. The diagnosis method presented here demonstrates plausible mechanisms that relate changes in precipitation, RH, and SAT under different climate perturbations. Therefore, uncertainty in future tropical precipitation changes may be linked with uncertainty in future RH and SAT changes.

1. Introduction

The Fifth Assessment Report of the Intergovernmental Panel on Climate Change (IPCC) outlines current projections of tropical precipitation change under anthropogenic global warming (Collins et al. 2013; Christensen et al. 2013). These projections are based on general circulation model (GCM) climate simulations from phase 5 of the Coupled Model Intercomparison Project (CMIP5). Despite modeling improvements since earlier phases of CMIP, persistent intermodel disagreement contributes to uncertainty in patterns of policy-relevant regional and local precipitation change (Knutti and Sedláček 2013).

Tropical precipitation change under global warming is typically partitioned into thermodynamic and dynamic contributions (Vecchi and Soden 2007; Seager et al. 2010). Thermodynamic changes comprise Clausius–Clapeyron-related increases in moisture at 7% K^{-1} of global mean warming. Dynamic changes are related to changes in atmospheric circulation, such as spatial shifts in convection (Chadwick et al. 2013), enhancement and narrowing of the intertropical convergence zone (ITCZ) (Lau and Kim 2015; Byrne and Schneider 2016), and Hadley cell expansion (Seidel et al. 2008). A tropical mean circulation weakening, largely due to restricted increases in tropospheric radiative cooling in descent regions, is a robust feature of global warming simulations (Vecchi and Soden 2007). Thermodynamic increases, modulated by circulation weakening, lead to a large-scale wet-get-wetter pattern of precipitation change (Held and Soden 2006). On smaller scales, spatial shifts dominate tropical precipitation changes (Chadwick et al. 2013). These precipitation shifts can be linked with a number of mechanisms, such as sea surface temperature (SST) pattern change (Xie et al. 2010),

land–sea temperature contrast changes, plant physiological changes, and direct responses to carbon dioxide (Chadwick et al. 2017). However, a simplified theory for understanding the mechanisms contributing to these shifts, and linking precipitation changes over land and ocean, is currently lacking in the literature.

In equatorial regions, horizontal temperature and density gradients are very weak above the boundary layer because of a small Coriolis parameter and, therefore, small rotational effects (Charney 1963). Consequently, the primary energy balance on local scales is between vertical advection and diabatic heating. To first order, the free-tropospheric temperature profile can be assumed to be uniform across the tropics. Sobel et al. (2001) term this assumption the weak temperature gradient (WTG) approximation and present a simplified theory for the tropical circulation. Sobel and Bretherton (2000) demonstrated how uncoupled single-column models, prescribed with varying surface temperatures and identical free-tropospheric temperature profiles, simulate a climatological precipitation pattern similar to that of a full GCM. Further theoretical and modeling studies demonstrated the suitability of the WTG approximation for representing idealized Walker- (Bretherton and Sobel 2002) and Gill–Matsuno-type (Bretherton and Sobel 2003) circulations.

Lambert et al. (2017) present a simplified method for diagnosing tropical precipitation change following the WTG approximation. Assuming relatively uniform free-tropospheric temperature profiles, convective initiation is strongly linked with surface conditions (Sobel et al. 2001). This forms the basis of the Lambert et al. (2017) method: local precipitation depends only on the local relative humidity (RH) and surface air temperature (SAT), relative to the tropical mean RH and SAT, respectively. Therefore, precipitation shifts can be characterized by surface changes in RH and SAT, relative to their tropical means. A physical justification for this simplification is presented by Xie et al. (2010) in the form of an idealized two-layer model of tropical moist stability. Moist static energy (MSE) is largely uniform in the tropical free troposphere because of weak horizontal temperature gradients and relatively low moisture above the boundary layer. Hence, the difference between MSE at the surface and in the free troposphere, which influences convection and therefore precipitation, is mainly controlled by MSE variations at the surface. SAT or surface RH increases would decrease moist stability, enhancing or initiating convection. Surface RH changes could also affect convective initiation by changing the height of the lifting condensation level. Free-tropospheric increases in environmental RH would enhance convection via entrainment into convective plumes (Sobel et al. 2001). Although not explicitly included in the Lambert et al. (2017) method, lower-tropospheric RH is likely to be spatially and temporally correlated with surface RH, so the method may implicitly include information about the humidity of entrained environmental air.

In this study, we analyze the performance of the Lambert et al. (2017) method at diagnosing observed present-day shifts in tropical rainfall associated with El Niño–Southern Oscillation (ENSO). ENSO is the leading mode of interannual climate variability, with atmosphere–ocean feedbacks linking SST anomalies and precipitation in the tropical Pacific and teleconnections leading to tropical and extratropical weather impacts (McPhaden et al. 2006). ENSO-related precipitation anomalies are evident in recent observations, reanalyses, and a variety of present-day CMIP5 climate model simulations (Bellenger et al. 2014). Therefore, we consider predicting ENSO precipitation shifts for a range of data sources to be a necessary test of the Lambert et al. (2017) method.

The first question to guide our analysis is this: Does the Lambert et al. (2017) method adequately diagnose present-day ENSO precipitation shifts? A key finding of Lambert et al. (2017) is the substantial intermodel variability in the diagnosis method performance for global warming–driven precipitation changes in an ensemble of CMIP5 model simulations. This motivates a second question: What factors influence the performance of the diagnosis method for ENSO and global warming precipitation shifts? The remainder of this paper is structured as follows. In section 2, we describe the data sources used, and in section 3, we explain our implementation of the Lambert et al. (2017) method. ENSO representation and diagnosed shifts for observations and climate model simulations are discussed in sections 4 and 5. In section 6, we examine relationships between ENSO and global warming–diagnosed precipitation changes, and finally, section 7 presents our conclusions.

2. Data

a. Observations—Precipitation

The source for monthly mean precipitation observations is the Global Precipitation Climatology Project (GPCP) version 2.3 dataset (Adler et al. 2003). The GPCP dataset combines both satellite and in situ precipitation gauge measurements and has spatially complete coverage at $2.5° \times 2.5°$ resolution. Present-day observations between January 1979 and December 2008 are used in this study because this coincides with the

TABLE 1. El Niño and neutral composite descriptions for piControl and spatial correlations for the 18 CMIP5 models used in this study. For amip, the CanAM4 and HadGEM2-A configurations were used in place of CanESM2 and HadGEM2-ES, respectively. (Expansions of acronyms are available online at http://www.ametsoc.org/PubsAcronymList. In addition, GCESS is the College of Global Change and Earth System Science at BNU, MOHC is the Met Office Hadley Centre, and NCC is the Norwegian Climate Centre.)

Model (amip configuration)	Institution	piControl periods		Diagnosed vs simulated spatial correlation		
		El Niño	Neutral	amip El Niño	piControl El Niño	Global warming
ACCESS1.0	CSIRO–BoM	7	14	0.63	0.70	0.46
ACCESS1.3	CSIRO–BoM	7	18	0.62	0.63	0.71
BNU-ESM	GCESS	12	5	0.78	0.71	0.59
CanESM2 (CanAM4)	CCCma	10	9	0.79	0.69	0.61
CCSM4	NCAR	10	7	0.66	0.72	0.30
CNRM-CM5	CNRM–CERFACS	8	12	0.67	0.72	0.47
CSIRO Mk3.6.0	CSIRO–QCCCE	3	19	0.68	0.67	0.81
FGOALS-s2	LASG/IAP	10	8	0.71	0.66	0.41
GFDL CM3	NOAA/GFDL	7	13	0.70	0.74	0.47
GISS-E2-R	NASA GISS	6	18	0.68	0.61	0.61
HadGEM2-ES (HadGEM2-A)	MOHC	7	15	0.62	0.71	0.47
INM-CM4.0	INM	4	20	0.51	0.51	0.38
IPSL-CM5A-LR	ISPL	7	16	0.71	0.75	0.35
IPSL-CM5A-MR	ISPL	7	12	0.71	0.75	0.42
IPSL-CM5B-LR	ISPL	9	11	0.70	0.82	0.48
MIROC5	MIROC	8	10	0.74	0.87	0.65
MRI-CGCM3	MRI	4	17	0.80	0.76	0.66
NorESM1-M	NCC	11	10	0.77	0.77	0.38
MME mean	—	—	—	0.78	0.82	0.64

range of the atmosphere-only amip experiment for the CMIP5 ensemble.

b. Reanalysis—Temperature and relative humidity

For reanalysis data, the European Centre for Medium-Range Weather Forecasts (ECMWF) interim reanalysis (ERA-Interim) (Dee et al. 2011) is used. ERA-Interim is constructed by prescribing observed SST and land surface conditions and assimilating observations into an atmosphere GCM. Monthly mean SAT is available directly. Monthly mean RH cannot be estimated directly from monthly means of temperature and dewpoint temperature because of the nonlinear relationship between temperature and specific humidity. Therefore, daily RH is estimated using daily reanalysis of surface air temperature and dewpoint temperature and Eq. (7.5) presented in ECMWF (2016). The mean of these daily values for each month provides the monthly mean RH. All ERA-Interim data are interpolated onto the GPCP 2.5° grid. In this analysis, we term ERA-Interim SAT and RH and GPCP observed precipitation as ERA-Interim–GPCP.

c. CMIP5 model simulations

Monthly mean simulated surface air temperature, RH, and precipitation from the first ensemble member (r1i1p1) of 18 CMIP5 models are used, as listed in Table 1. We examine the multimodel ensemble (MME) present-day simulations between 1979 and 2008 from the amip

experiment, where the observed monthly mean SST conditions are prescribed. Additionally, we use the coupled piControl experiment, where greenhouse gas forcing and aerosol concentrations are fixed at preindustrial levels, and the temporal evolution of the atmosphere and ocean are simulated. To explore idealized global warming changes, we compare piControl with the abrupt4xCO2 simulations, following Lambert et al. (2017). The abrupt4xCO2 experiment involves instantaneously quadrupling the concentration of atmospheric carbon dioxide. For each model, we limit our analysis to the last 30 years of the long-running piControl and abrupt4xCO2 (years 121–150) simulations to remove any transient effects during spinup. Hereafter, we refer to abrupt4xCO2 minus piControl as global warming, for brevity. All model-simulated data are interpolated onto the GPCP 2.5° grid to enable intercomparison. Further details of the amip, piControl, and abrupt4xCO2 experiment designs are described by Taylor et al. (2012).

3. Methods

a. Constructing El Niño composites

We focus on the tropical region in the latitude band between 30°N and 30°S in this analysis. In each ENSO data source, we examine the 12-month periods between each July and the following June. This period is chosen because it represents the typical El Niño growth and decay stages and a variety of teleconnections

(Ropelewski and Halpert 1987). Each 12-month period is classified as either El Niño or neutral via the oceanic Niño index (ONI) (NOAA 2015). The ONI is based on spatial mean SST anomalies in the Niño-3.4 (5°N–5°S, 120°–170°W) region. The amplitude of anomalies in this region is commonly used to represent the magnitude of the oceanic component of an ENSO event (Trenberth and Stepaniak 2001). The ONI identifies an El Niño event if five consecutive and overlapping 3-month periods have a Niño-3.4 SST anomaly greater than + 0.5 K, a La Niña event if the SST anomaly is less than −0.5 K, and neutral conditions otherwise. In ERA-Interim–GPCP and the amip MME, eight El Niño and nine neutral events are identified from the prescribed SST conditions. In the piControl MME, there is a broad variety in the frequency of ENSO events, as detailed in Table 1. El Niño and neutral SAT, RH, and precipitation composites are constructed by calculating the mean of each of the El Niño and neutral periods, respectively.

b. Implementing the Lambert et al. method

A detailed description of the precipitation change diagnosis method is presented in Lambert et al. (2017). Consider one month in a control scenario: for instance, a neutral ENSO or piControl composite. The method proceeds by producing an ordered vector of gridpoint control RH and partitioning it into n equally sized bins ($n = 10$ is fixed in this study). Subsequently, within each RH bin, the ordered vector of gridpoint control SAT is partitioned into n equally sized bins, resulting in an $n \times n$ space of RH and SAT values. Figures 1a and 1b demonstrate the mean RH and SAT, respectively, within each bin for the ERA-Interim July–June composite means. We note that absolute RH increases with RH bin number from 60% to 82%, and this is relatively uniform within each SAT bin. This absolute RH increase with RH bin number is nonlinear, with the steepest gradient in low RH bins. In contrast, absolute SAT increases more linearly with SAT bin number but varies greatly across RH bins. For instance, mean SAT increases from 290 to 298 K and from 296 to 300 K in RH bins 2 and 9, respectively.

Subsequently, the mean control precipitation P_{ij} for grid points in RH bin i and SAT bin j is calculated (Fig. 1c provides an example for GPCP precipitation in ERA-Interim RH and SAT bins). Next, for one month in a perturbation scenario, such as an El Niño or abrupt4xCO2 composite, gridpoint RH and SAT is binned following the same procedure as the control scenario. Each tropical grid point is then a member of RH bins i and i' and SAT bins j and j' in the control and perturbation scenarios, respectively. The diagnosed

precipitation change ΔP at each grid point is then $\Delta P = sP_{i'j'} - P_{ij}$, where s is the fractional change in tropical mean precipitation. Hence, s largely represents the thermodynamic precipitation change, and spatial shifts in convection are diagnosed through changes in RH or SAT bins. Under global warming on a tropics-wide scale, the thermodynamic precipitation increase is opposed by a mean circulation weakening (Vecchi and Soden 2007), as discussed in the introduction. We note that other factors controlling tropical mean precipitation changes, such as poleward energy transport (Held and Soden 2006), are implicitly incorporated in this framework. The scaling factor s is expected to modulate the magnitude of precipitation changes under global warming (Chadwick et al. 2013) but to be less important during El Niño events, where tropical mean temperature and circulation changes are much smaller, compared to spatial variations (Neelin et al. 1998; McPhaden et al. 2006).

To remove the seasonal cycle, we calculate the temporal means of the observed or simulated and diagnosed precipitation anomaly composites. For ERA-Interim–GPCP and the amip and piControl simulations, the temporal means represent July–June, and for the global warming simulations, the temporal means represent January–December. To quantify the performance of the diagnosis method, we calculate the area-weighted gridpoint (spatial) correlation between the temporal means of the simulated and diagnosed anomalies. Spatial correlation is a commonly used performance metric in the assessment of climate models (Flato et al. 2013) and forecasts of spatial fields (Jolliffe and Stephenson 2012).

A primary assumption of the diagnosis method is that the precipitation pattern in RH–SAT space P_{ij} is relatively invariant between the control and perturbation scenarios, except for a scaling by the tropical mean precipitation change. In GPCP observations, the tropical mean precipitation decreases by 0.43% from neutral to El Niño composites. Figure 1c displays neutral and El Niño composite mean GPCP precipitation as a function of ERA-Interim RH–SAT bin number. The precipitation patterns appear similar for both composites, with a small decrease in the relatively warmest and most humid bins from neutral to El Niño, consistent with the tropical mean change. Therefore, there is evidence in observations to support the assumption that precipitation as a function of local RH and SAT, relative to the tropical mean, is largely invariant under present-day shifts.

For ERA-Interim–GPCP, Fig. 1c demonstrates that precipitation increases more rapidly with RH bin number, in comparison with SAT bin number. This highlights the nonlinear relationship between precipitation,
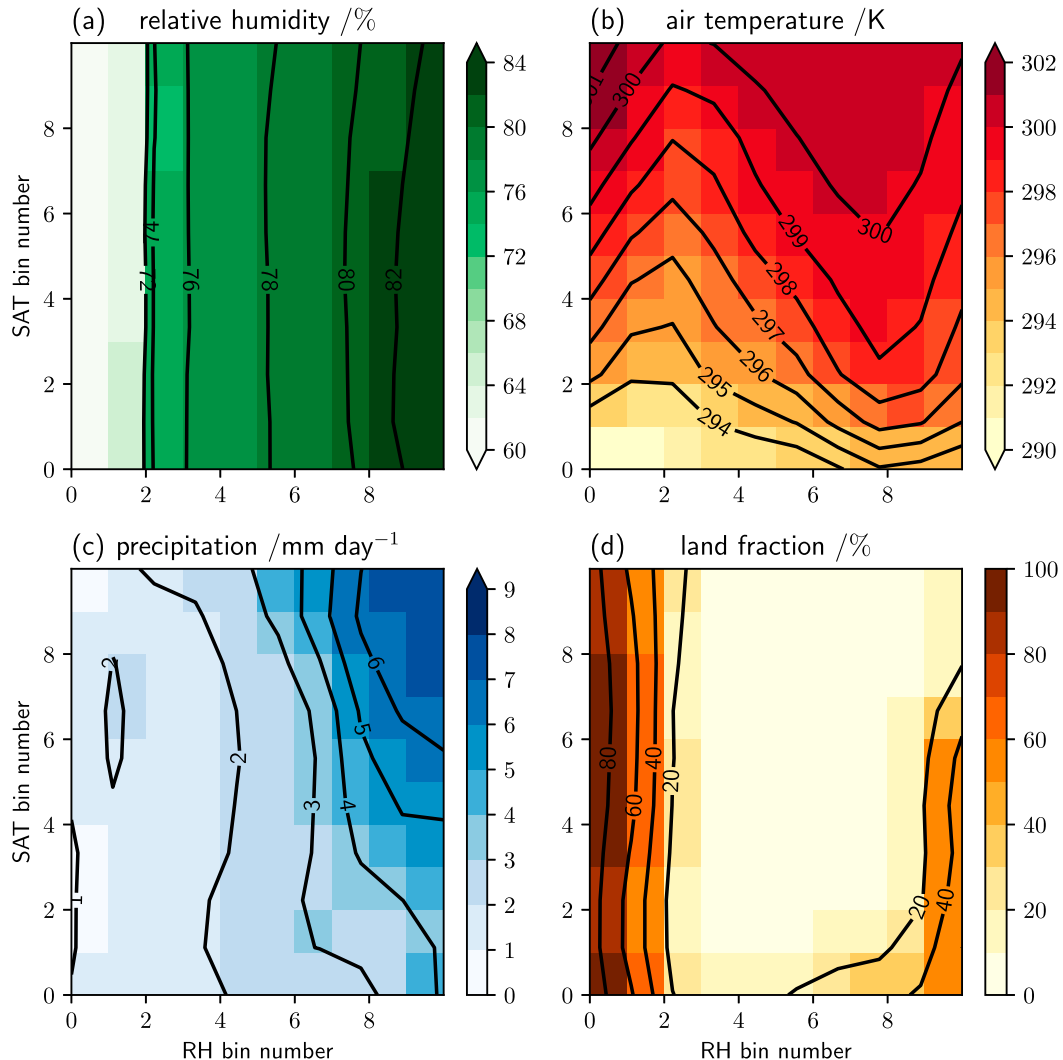
FIG. 1. Color shading shows the July–June neutral composite mean ERA-Interim (a) surface RH, (b) SAT, (c) GPCP precipitation, and (d) land fraction in each ERA-Interim RH–SAT bin. Black contours show the July–June El Niño composite means.

RH, and SAT. Under the WTG assumption, SAT bin number changes could alter the difference between the boundary layer and free-tropospheric temperature and, therefore, affect dry static stability. Similarly, RH bin number changes may affect vertical gradients in equivalent potential temperature and, hence, moist static stability. Consequently, changes in either SAT or RH bin numbers can be linked with precipitation changes. An implicit assumption of the Lambert et al. (2017) method is a spatial and temporal relationship between surface and lower-tropospheric RH. This is evident in ERA-Interim because there is a moderate spatial correlation between surface and 700-hPa El Niño RH anomalies over both land (0.57) and ocean (0.62). Consequently, surface RH bin number changes may

reflect free-tropospheric RH changes, leading to large changes in column water vapor (CWV) (Bretherton et al. 2004; Holloway and Neelin 2009). In observations (Schiro et al. 2016) and climate model simulations (Kuo et al. 2017), precipitation sharply increases above a CWV threshold over both land and ocean. Relatively high CWV increases entrainment of environmental moisture, deepening convection and leading to heavier precipitation. This mechanism may explain why precipitation increases more rapidly with RH bin number than with SAT bin number.

Comparing Fig. 1c with supplementary Fig. 1 of Lambert et al. (2017), we note that these results for ERA-Interim–GPCP are consistent with the majority of CMIP5 model piControl simulations, with the exception

of FGOALS-s2. In FGOALS-s2, the heaviest precipitation occurs in the highest SAT bin of middle-ranking RH bins. Figure 1d demonstrates that the majority of tropical land areas are classified either in the highest RH bin or the two lowest RH bins for both the El Niño and neutral ERA-Interim–GPCP composites. The presence of tropical land in the highest RH bin indicates that RH decreases could plausibly lead to a lowering of RH bin number for land grid points. This result is consistent with a number of the CMIP5 model piControl simulations. However, as discussed by Lambert et al. (2017), the FGOALS-s2, IPSL-CM5A-LR, and IPSL-CM5A-MR piControl experiments do not simulate significant areas of tropical land in the highest RH bin. This highlights an inconsistency between these model simulations and present-day conditions in ERA-Interim.

4. ENSO in observations and reanalysis

In present-day observations, ENSO events are characterized by anomalous warming in the eastern or central equatorial Pacific, leading to both tropical and extratropical precipitation shifts (McPhaden et al. 2006). Figures 2a and 2b demonstrate the ERA-Interim composite mean RH and SAT El Niño anomalies, respectively. The magnitude of RH changes is typically larger over land, in comparison to over ocean. A decrease in RH is observed over a majority of tropical land (62%) and ocean (53%) areas, including South America, southern Africa, the Sahel, Southeast Asia, Australia, and the subtropical Pacific. Furthermore, an increase in SAT is observed over a high proportion of tropical land (83%) and ocean (75%) areas. GPCP observed precipitation anomalies are displayed in Fig. 2c. Precipitation increases are evident over the western Indian Ocean, central and eastern equatorial Pacific, and eastern Asia. In addition, there are precipitation decreases over the tropical Maritime Continent, the western Pacific, South America, and the subtropical central Pacific.

There is a moderate spatial correlation between the El Niño precipitation and RH anomalies over ocean (0.51) and land (0.59), as well as an anticorrelation between El Niño RH and SAT anomalies over land (-0.56). The magnitude of spatial correlations between anomalous precipitation and SAT are weaker over both land (-0.43) and ocean (0.41). These spatial correlations are qualitatively consistent with temporal correlations for in situ observation sites (Pfhal and Neidermann 2011). Over both land and ocean, ENSO circulation and precipitation changes lead to surface RH changes through changes in moisture advection and re-evaporation in the boundary layer. Additionally, RH changes over land can

be linked with soil moisture changes that feedback on evaporation and precipitation and with moisture advection from neighboring ocean regions (Chadwick et al. 2016; Byrne and O'Gorman 2016).

Applying the Lambert et al. (2017) method using ERA-Interim El Niño changes in RH and SAT bin numbers and GPCP precipitation, the El Niño precipitation change is diagnosed. Figure 2d shows the spatial pattern of the diagnosed precipitation change (cf. Fig. 2c showing the observed precipitation change). The spatial correlation between the observed and diagnosed tropical changes is 0.69 (0.71 over ocean, 0.46 over land), suggesting moderately good performance, especially over ocean grid points. In addition, we note that the signs of the large-scale features are correctly diagnosed: increased precipitation in the western Indian Ocean and the central and eastern Pacific Ocean, and decreased precipitation over the eastern Indian Ocean, the Maritime Continent, and equatorial South America. However, there is a general underestimation of the magnitude of the precipitation anomalies. Regressing the diagnosed changes on the observed precipitation changes, the slope estimate is 0.41, with a 95% confidence interval of [0.40, 0.43]. This is consistent with the weaker magnitudes of diagnosed, compared to simulated, global warming shifts, as presented in Lambert et al. (2017). A reason for the weaker diagnosed magnitudes is the aggregation process in the diagnosis method because bin averaging smooths precipitation as a function of RH and SAT relative to their tropical means.

Differences in diagnosis performance over land and ocean are related to how closely the tropical troposphere satisfies the assumptions of the Lambert et al. (2017) method. The ocean surface is essentially flat and homogeneous, in contrast to orographic, vegetation, and soil moisture variations over land. These surface attribute differences lead to spatial variability in latent and sensible heating over land, affecting boundary layer dynamics. For example, there is a significantly stronger diurnal cycle of convective intensity over land, in comparison to over ocean, linked with enhanced boundary layer destabilization following daytime surface heating (Nesbitt and Zipser 2003). Differences in aerosol constituents over land and ocean may also affect convection via microphysical processes and their effects on buoyancy (Rosenfeld et al. 2008). Consequently, several competing processes modulate conditional instability and, hence, deep convection over land and ocean (Schiro et al. 2016). Furthermore, over the Amazon and Congo basins, sparse observational coverage may increase uncertainty in ERA-Interim (Cowtan and Way 2014). This observational uncertainty may contribute to weaker diagnosis performance over these areas.
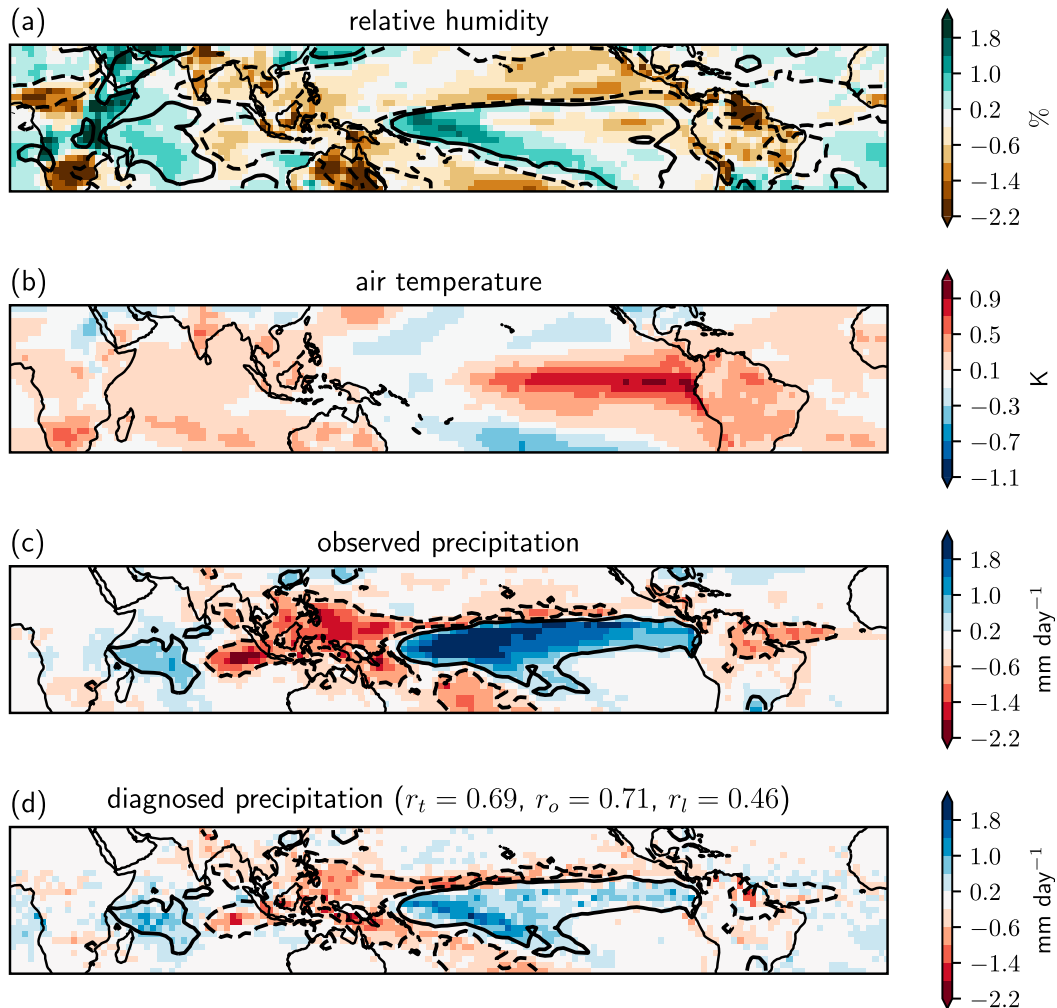
FIG. 2. Color shading shows the July–June composite mean (El Niño minus neutral) anomalies: ERA-Interim (a) surface RH, (b) SAT, (c) GPCP precipitation, and (d) diagnosed precipitation from the Lambert et al. (2017) method. Black contours in (a) indicate the −1% (dashed) and +1% (solid) 700-hPa relative humidity anomaly, and in (c) and (d) indicate the −0.5 (dashed) and 0.5 (solid) mm day^{-1} GPCP precipitation anomaly. Spatial correlations between the observed and diagnosed precipitation anomalies for tropical, oceanic, and land grid points are denoted by r_t, r_o, and r_l, respectively.

Boundary layer variations over land may lead to horizontal temperature gradients in the lower troposphere, compromising the WTG approximation. This suggestion is supported by Fig. 3, showing the seasonal magnitude of the ERA-Interim zonal mean horizontal temperature gradient at 500 hPa $|\nabla T|$. Between 15° and 30°N, $|\nabla T|$ is larger over land in both neutral and El Niño composites. The difference between land and ocean $|\nabla T|$ is especially large during Northern Hemisphere autumn and winter, as shown by Figs. 3a and 3b. Generally, in all seasons, the magnitude of horizontal temperature gradients, which are largely meridional, increases poleward from the equator. Because there is more land than ocean between 20° and 30°N, there is a larger fraction of land

grid points where the WTG approximation is only weakly satisfied, and variations in free-tropospheric moisture may be relatively large.

As discussed in section 3b, an implicit assumption of the diagnosis method is a link between surface and lower-tropospheric RH. There is evidence of this link in ERA-Interim, where 63% and 66% of tropical land and ocean areas, respectively, have a correlation in temporal variability between surface and 700-hPa RH greater than 0.5. Areas with low or anticorrelation are subtropical Africa, Australia, and South America. These regions are typically climatological descent regions, with weak vertical mixing and relatively high stratification (Sherwood et al. 2010). Examining Fig. 2a, there is evidence
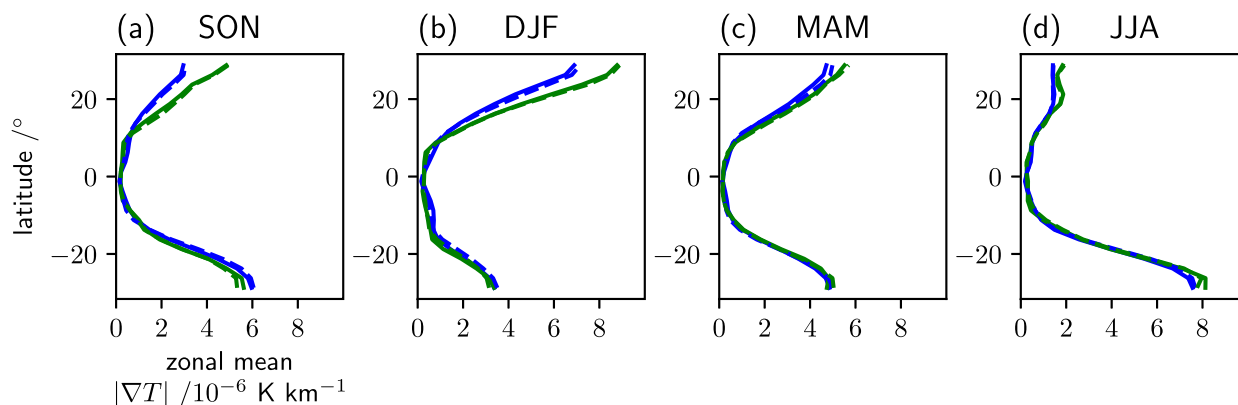
FIG. 3. Zonal mean magnitude of the ERA-Interim horizontal temperature gradient at 500 hPa $|\nabla T|$ vs latitude for each season. Blue lines indicate the neutral (solid) and El Niño (dashed) composite means over ocean grid points. Green lines indicate the neutral (solid) and El Niño (dashed) composite means over land grid points.

of spatial variability in the link between surface and 700-hPa RH El Niño anomalies. There is large-scale sign agreement over much of tropical Africa, the equatorial Indian Ocean, the western and central Pacific Ocean, and tropical South America. However, there is weaker sign agreement, or disagreement, over the equatorial eastern Pacific and western Atlantic Oceans. These areas demonstrate relatively weak diagnosis performance in Fig. 2d, with the magnitude of the precipitation changes generally underestimated.

To assess the relative influence of RH and SAT changes in diagnosis performances, we examine four new configurations of the Lambert et al. (2017) method. First, we bin (ENSO) neutral precipitation using neutral RH and use the El Niño change in RH bin numbers to diagnose the El Niño change in precipitation. This configuration is termed ''RH 1D'' because it uses only one surface variable (RH). A second, corresponding configuration, ''SAT 1D,'' uses El Niño SAT bin number changes to diagnose the precipitation change. A third configuration involves binning neutral precipitation using both RH and SAT (as described in section 3b) and using the El Niño change in RH bin number, as well as the neutral SAT bin number, to diagnose the El Niño precipitation change. This configuration is termed ''RH partial 2D'' because it considers El Niño changes in only one of two surface variables (RH). The fourth configuration, ''SAT partial 2D,'' uses El Niño SAT bin number changes and neutral precipitation binned on RH and SAT to diagnose precipitation changes. For completeness, we refer to the original configuration as 2D for the remainder of this study.

Diagnosed precipitation changes for the four new configurations are presented in Fig. 4. Both the RH 1D and partial 2D configurations diagnose a precipitation pattern similar to the 2D configuration, as displayed in Fig. 2d. In contrast, the SAT 1D and partial 2D configurations

diagnose a markedly different precipitation change pattern. The SAT 1D and partial 2D methods diagnose increases in the eastern equatorial Pacific as a result of the relatively strong surface warming associated with El Niño SST changes. The RH 1D diagnosis method performs considerably better (0.56) than the SAT 1D method (0.27) over both land and ocean grid points. In particular, the SAT 1D diagnosed precipitation changes are weakly anticorrelated (-0.28) with the observed changes, while the RH 1D changes are positively correlated (0.51). Comparable differences in the performance of the RH (0.62) and SAT (0.39) partial 2D configurations are also demonstrated. These results suggest that observed precipitation changes are more strongly linked with RH bin number changes, in comparison with SAT bin number changes. In particular, both the RH 1D and RH partial 2D configurations over land perform equivalently well (0.51) and better than the 2D method (0.46), which uses changes in RH and SAT bin numbers. We note that the relative importance of RH changes, in comparison with SAT changes, is only weakly linked with relative contributions to low-level MSE changes, as discussed in appendix A.

The sum of the partial 2D changes, RH partial 2D plus SAT partial 2D, represents the diagnosed precipitation change due to independent changes in RH and SAT bin numbers. This sum is strongly correlated (0.96) and linearly related with the 2D diagnosed change, as shown by Fig. 5a. Similarly, the sum of the 1D changes, RH 1D plus SAT 1D, is well correlated (0.75) with the 2D diagnosed changes. This indicates that for the majority of grid points, precipitation changes are linked with either RH or SAT bin number changes. Additionally, given the base state SAT or RH bin in each case, the diagnosis performance improves. The magnitudes of the differences between the 2D changes and the sum of the partial 2D changes, as displayed in Fig. 5b, are typically small ($<0.5\,\mathrm{mm\,day^{-1}}$) across the tropics. In a small area of the
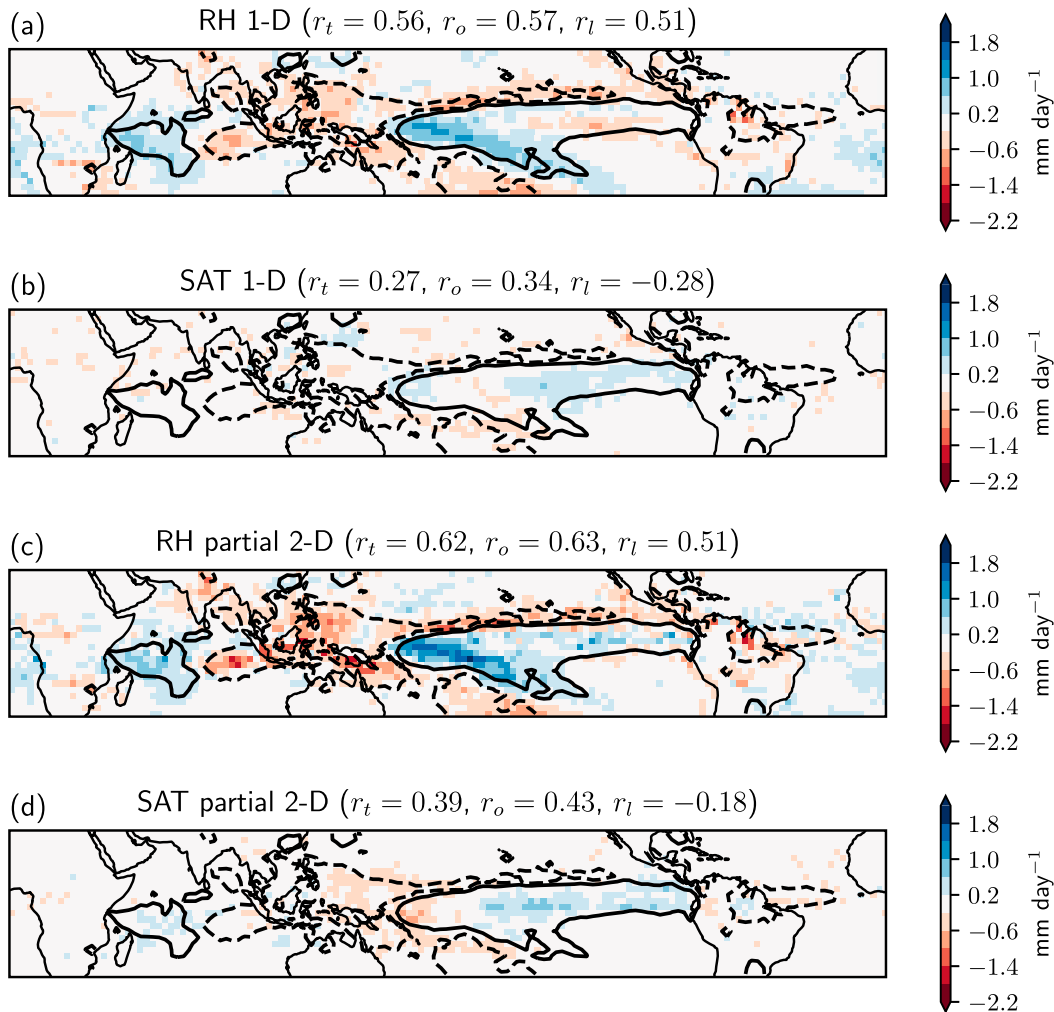
FIG. 4. Color shading shows the July–June mean diagnosed precipitation anomaly for four configurations of the Lambert et al. (2017) method: (a) 1D using RH changes, (b) 1D using SAT changes, (c) partial 2D using RH changes, and (d) partial 2D using SAT changes. Black contours indicate the -0.5 (dashed) and 0.5 (solid) mm day^{-1} GPCP precipitation anomaly, and r_t, r_o, and r_l are as in Fig. 2.

central equatorial Pacific, both RH and SAT bin numbers increase, leading to a large increase in precipitation, which is underestimated by independent changes in RH and SAT bin numbers. This demonstrates how the 2D and partial 2D methods capture the nonlinear relationship between precipitation, RH, and SAT bin changes.

5. ENSO in climate model simulations

In section 4, we demonstrated that the Lambert et al. (2017) method performs fairly well at diagnosing ENSO precipitation shifts in present-day observations and reanalysis. In this section, we examine whether consistent performance is evident for climate model ENSO simulations. Specifically, we test atmosphere-only (amip) and

coupled (piControl) experiments for a multimodel ensemble of 18 climate models contributing to CMIP5.

The spatial correlation between simulated and diagnosed amip El Niño precipitation anomalies is 0.78 for the MME mean and ranges between 0.51 and 0.8 for individual models. For piControl El Niño precipitation anomalies, the MME mean spatial correlation is 0.82, and for individual models, correlations range between 0.5 and 0.87. Hence, for both experiments in all models, the method performs relatively well at diagnosing El Niño precipitation shifts. The MME mean patterns of SAT, RH, and precipitation are smoother than those of individual models. This is likely to contribute to the high performance of the MME mean for both experiments, relative to the individual models. For comparison, the
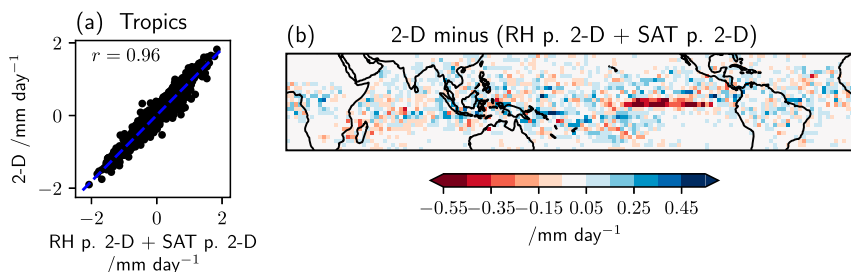
FIG. 5. (a) ERA-Interim–GPCP July–June mean 2D diagnosed precipitation changes vs the sum of the RH partial 2D and SAT partial 2D diagnosed precipitation changes, with the blue dashed line indicating the regression slope. (b) 2D diagnosed precipitation changes minus the sum of the RH partial 2D and SAT partial 2D diagnosed precipitation changes. Note the smaller range of the color scale, in comparison to Fig. 4.

spatial correlation between observed and predicted ERA-Interim–GPCP El Niño precipitation anomalies is 0.69. Therefore, the diagnosis performance of ERA-Interim–GPCP lies within both the amip and piControl MME variability.

Consistent with ERA-Interim–GPCP observations, the diagnosis method performs better over ocean than land in each model and the MME mean for both the amip and piControl El Niño simulations. The majority of models, in both experiments, simulate a decrease in precipitation over the eastern Amazon basin, which agrees well with GPCP observations. In these climate model simulations and observations, the diagnosis method typically underestimates the magnitude and spatial extent of this precipitation decrease, diminishing the overall land performance. The observed El Niño precipitation decreases over southern Africa, and increases over eastern China and equatorial Africa are only weakly simulated by the MME, especially in the piControl experiment. Hence, the simulated precipitation change signal over the majority of tropical land areas is relatively weak. As discussed in section 4, a number of factors affect boundary layer dynamics, modulating deep convection differently over land and ocean and influencing diagnosis performance. Differences in the suitability of the Lambert et al. (2017) method assumptions contribute to the varying disparity in land and ocean diagnosis performance for each model.

Examining Fig. 6, the amip simulated El Niño precipitation anomalies are similar to the GPCP observed precipitation anomaly (see Fig. 2c). There is moderate intermodel variability in the simulated precipitation anomalies, especially over tropical Africa and South America. This variability is likely to be linked with differences in atmospheric simulation. However, the key observed features and good diagnosis performance are evident in all models. For example, each model simulates a precipitation increase (>0.5 mm day^{-1}) in the central and

eastern equatorial Pacific and a precipitation decrease (<−0.5 mm day^{-1}) in the western and off-equatorial Pacific. The Lambert et al. (2017) method adequately predicts this shift in precipitation for each model, given the simulated El Niño changes in RH and SAT.

The coupled model piControl simulated and diagnosed El Niño precipitation anomalies are displayed in Fig. 7. There is greater intermodel variability in these patterns, in comparison with the amip simulations and diagnoses. This increased variability is due to model differences in simulated El Niño SST anomalies and ocean–atmosphere feedbacks (Guilyardi et al. 2009). Despite this variability, the Lambert et al. (2017) diagnosis method performs relatively well at diagnosing El Niño precipitation changes across the tropics in each model. Moreover, the MME range of spatial correlations between simulated and diagnosed precipitation changes is similar for both prescribed SST (atmosphere only) and coupled (atmosphere–ocean) experiments. This suggests that the Lambert et al. (2017) method is flexible and capable of diagnosing shifts linked with a variety of El Niño SST anomalies.

Intermodel variability in the diagnosis performance is linked with how well each model satisfies the method assumptions, as outlined in section 3b. There is a significant correlation in intermodel variability between amip and piControl El Niño diagnosis performance across the tropics (0.63) and over tropical ocean grid points (0.64). To support these correlations, Fig. 8 displays scatterplots of amip versus piControl diagnosis performance. There is evidence of a positive linear association in performance between the atmosphere-only and the coupled experiments over ocean. This indicates that the performance of the Lambert et al. (2017) method over ocean grid points is relatively independent of how the model simulates SST, so atmospheric processes are the main source of model differences in diagnosis performance over ocean.
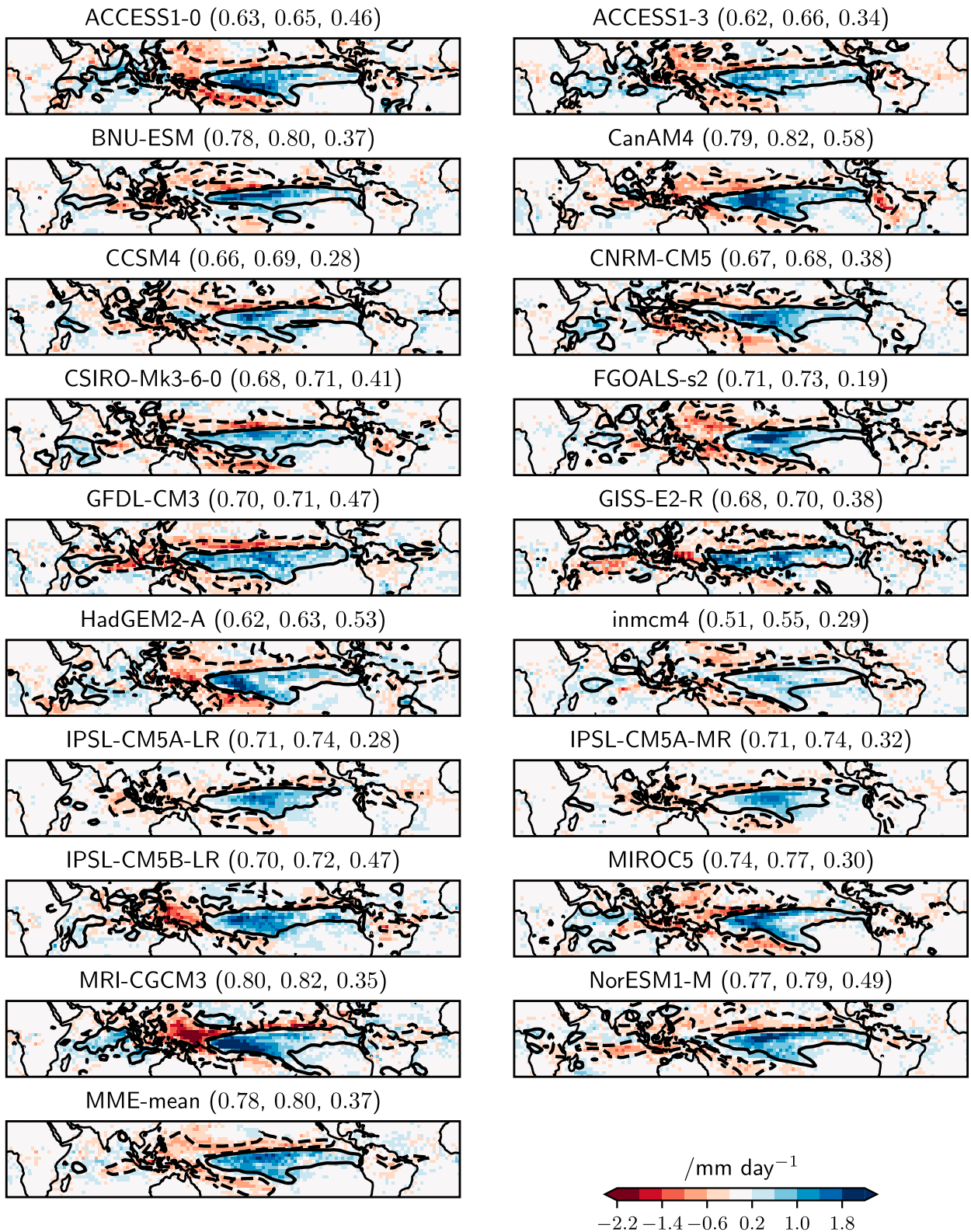
ACCESS1-0 (0.63, 0.65, 0.46)

ACCESS1-3 (0.62, 0.66, 0.34)

BNU-ESM (0.78, 0.80, 0.37)

CanAM4 (0.79, 0.82, 0.58)

CCSM4 (0.66, 0.69, 0.28)

CNRM-CM5 (0.67, 0.68, 0.38)

CSIRO-Mk3-6-0 (0.68, 0.71, 0.41)

FGOALS-s2 (0.71, 0.73, 0.19)

GFDL-CM3 (0.70, 0.71, 0.47)

GISS-E2-R (0.68, 0.70, 0.38)

HadGEM2-A (0.62, 0.63, 0.53)

inmcm4 (0.51, 0.55, 0.29)

IPSL-CM5A-LR (0.71, 0.74, 0.28)

IPSL-CM5A-MR (0.71, 0.74, 0.32)

IPSL-CM5B-LR (0.70, 0.72, 0.47)

MIROC5 (0.74, 0.77, 0.30)

MRI-CGCM3 (0.80, 0.82, 0.35)

NorESM1-M (0.77, 0.79, 0.49)

MME-mean (0.78, 0.80, 0.37)

/mm day^{-1}

−2.2 −1.4 −0.6 0.2 1.0 1.8

FIG. 6. Color shading shows amip El Niño diagnosed precipitation anomalies for 18 models and the MME mean. Dashed and solid contours indicate the simulated -0.5 mm day^{-1} and 0.5 mm day^{-1} precipitation, respectively. The triplet in parentheses (r_t, r_o, r_l) indicates the spatial correlation over the tropical, oceanic, and land grid points, respectively.
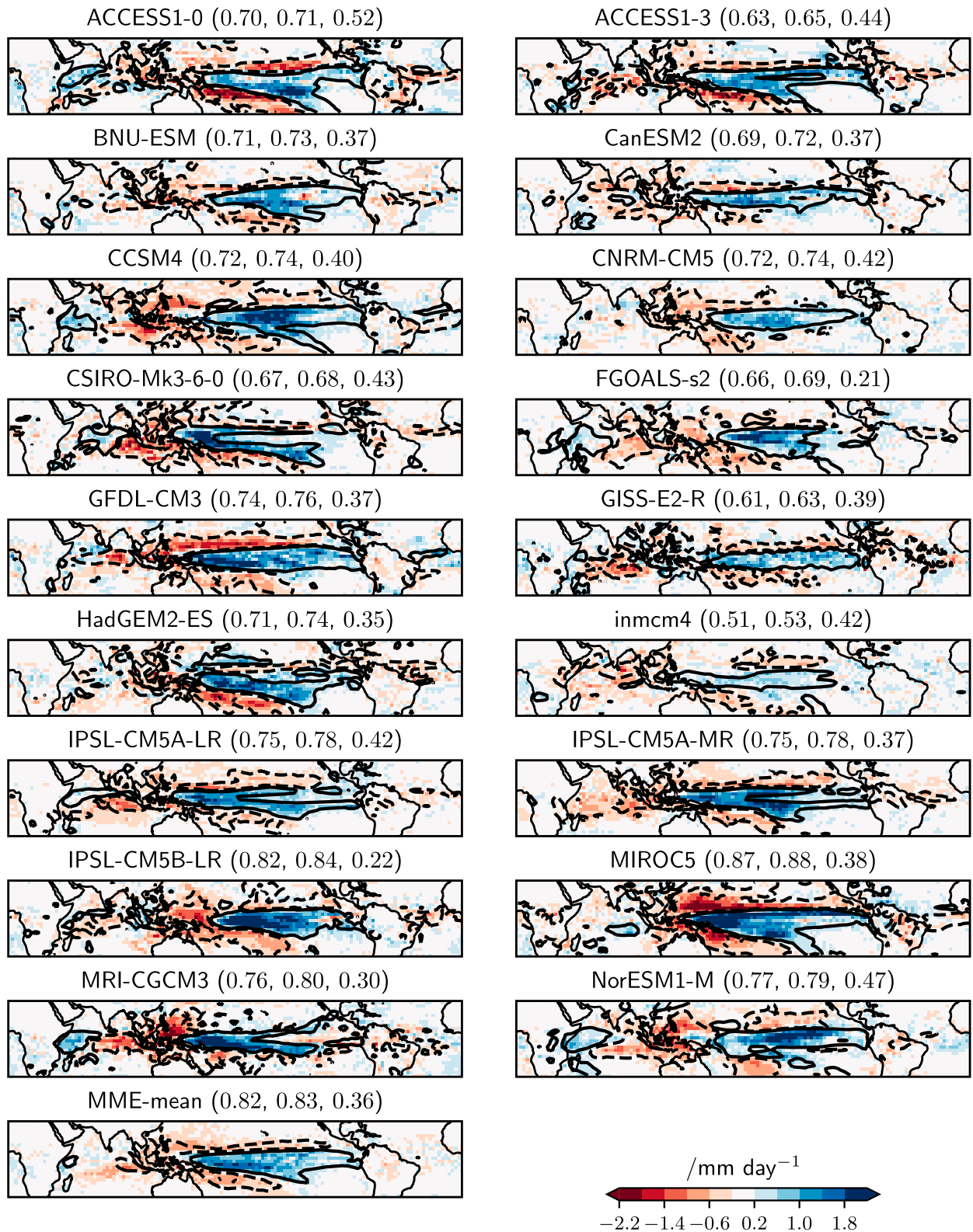
ACCESS1-0 (0.70, 0.71, 0.52)   ACCESS1-3 (0.63, 0.65, 0.44)

BNU-ESM (0.71, 0.73, 0.37)   CanESM2 (0.69, 0.72, 0.37)

CCSM4 (0.72, 0.74, 0.40)   CNRM-CM5 (0.72, 0.74, 0.42)

CSIRO-Mk3-6-0 (0.67, 0.68, 0.43)   FGOALS-s2 (0.66, 0.69, 0.21)

GFDL-CM3 (0.74, 0.76, 0.37)   GISS-E2-R (0.61, 0.63, 0.39)

HadGEM2-ES (0.71, 0.74, 0.35)   inmcm4 (0.51, 0.53, 0.42)

IPSL-CM5A-LR (0.75, 0.78, 0.42)   IPSL-CM5A-MR (0.75, 0.78, 0.37)

IPSL-CM5B-LR (0.82, 0.84, 0.22)   MIROC5 (0.87, 0.88, 0.38)

MRI-CGCM3 (0.76, 0.80, 0.30)   NorESM1-M (0.77, 0.79, 0.47)

MME-mean (0.82, 0.83, 0.36)

/mm day^{-1}

−2.2 −1.4 −0.6 0.2 1.0 1.8

FIG. 7. As in Fig. 6, but for piControl El Niño diagnosed precipitation anomalies.
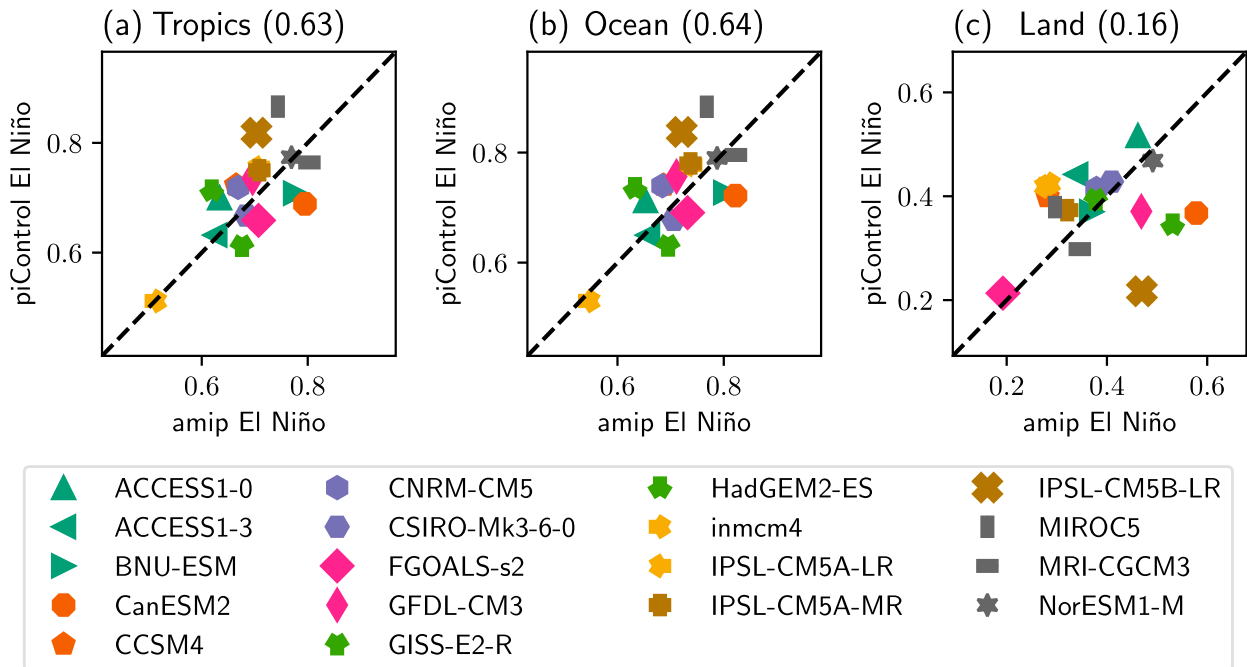
FIG. 8. Spatial correlations between simulated and diagnosed precipitation anomalies for July–June mean amip El Niño vs piControl El Niño, over the (a) tropics, (b) tropical oceans, and (c) tropical land. The dashed black line indicates the 1:1 diagonal.

Comparing amip and piControl diagnosis performance over land, the correlation in intermodel variability is much weaker (0.16), and Fig. 8c suggests there is little evidence of a linear relationship. Several factors may contribute to this inconsistency, in comparison with amip and piControl performance over ocean. Diagnosis performance over land is uniformly weaker than performance over ocean in observations, as discussed in section 4. Therefore, the smaller magnitude of the spatial correlations may inhibit any clear relationship in performance between the amip and piControl diagnoses. In addition, there is larger intermodel variability of El Niño teleconnection patterns over land in piControl simulations, in comparison with amip simulations, as displayed in Figs. 6 and 7. Consequently, amip and piControl El Niño precipitation shifts may be located over areas where the suitability of the WTG approximation changes.

6. Relating ENSO and global warming precipitation change diagnoses

In this section, we extend our analysis of the Lambert et al. (2017) method to examine the diagnosis performance for simulated global warming precipitation changes. We note that the tropical mean precipitation changes under global warming (6.0% for the MME mean) are substantially larger than El Niño–related changes (0.1% for the amip MME mean). This highlights the

importance of the thermodynamic scaling when applying the diagnosis method to simulated global warming precipitation changes.

Spatial correlations between simulated and diagnosed global warming precipitation anomalies range between 0.30 and 0.81 for individual models, and the MME mean spatial correlation is 0.64. Hence, there is a broader intermodel range of performance for global warming, in comparison with amip and piControl El Niño diagnosed precipitation changes. Figure 9 displays the simulated and diagnosed global warming precipitation anomalies for each model in the MME. We note large intermodel variability in the sign of precipitation changes, especially over tropical Africa and the Maritime Continent. However, the majority of models indicate precipitation increases over the equatorial Pacific and decreases over tropical South America. Model differences in SST pattern change and convergence zone shifts contribute to this intermodel variability in simulated precipitation change (Xie et al. 2010; Chadwick et al. 2013), as discussed in the introduction.

Similar to El Niño observations and climate model simulations, diagnosis performance is weaker over land, in comparison to over ocean, for the majority of the MME for global warming simulations. A number of models, such as CNRM-CM5 and CSIRO Mk3.6.0, simulate small precipitation changes over tropical land. Other models, such as GFDL CM3, GISS-E2-R,
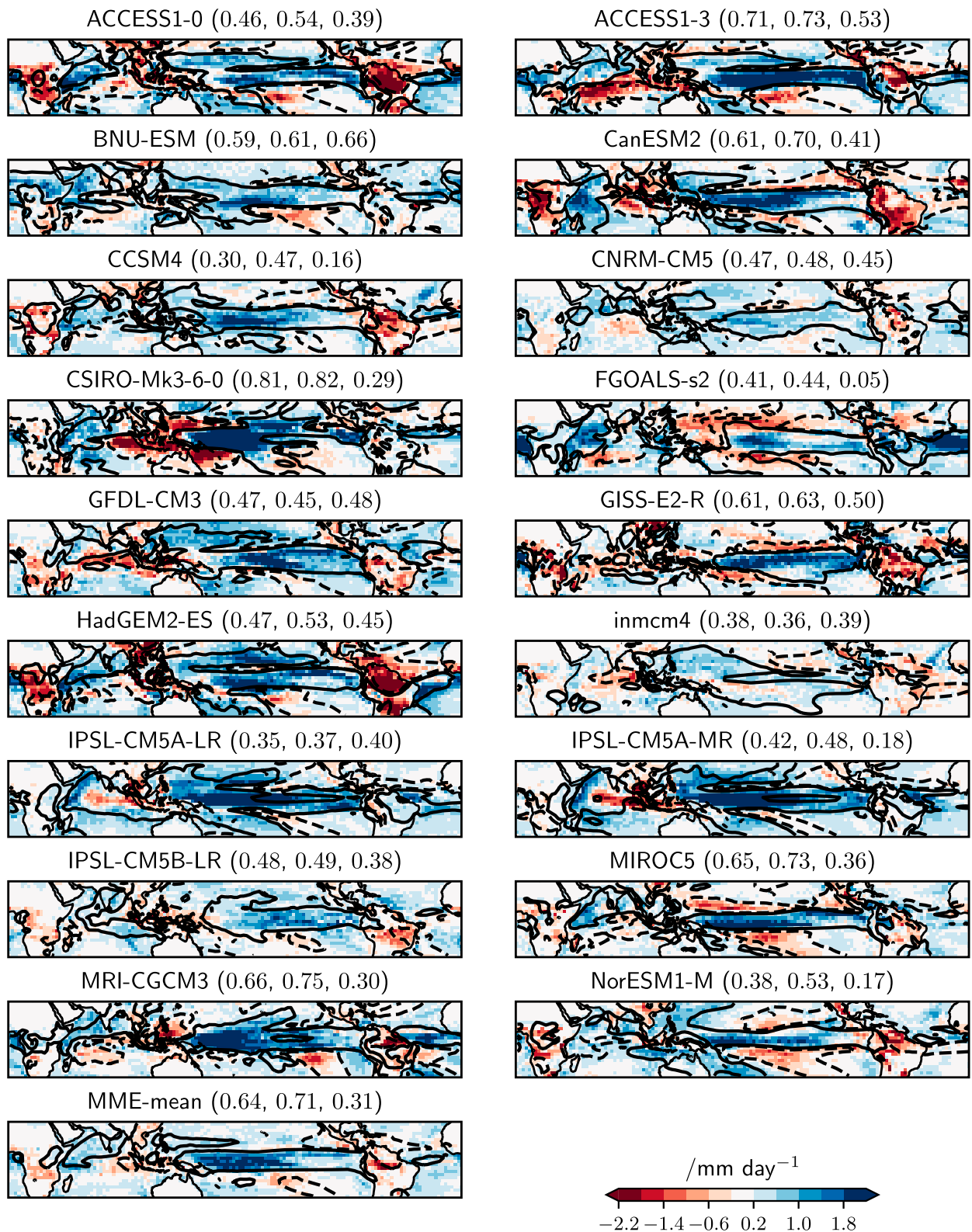
ACCESS1-0 (0.46, 0.54, 0.39)

ACCESS1-3 (0.71, 0.73, 0.53)

BNU-ESM (0.59, 0.61, 0.66)

CanESM2 (0.61, 0.70, 0.41)

CCSM4 (0.30, 0.47, 0.16)

CNRM-CM5 (0.47, 0.48, 0.45)

CSIRO-Mk3-6-0 (0.81, 0.82, 0.29)

FGOALS-s2 (0.41, 0.44, 0.05)

GFDL-CM3 (0.47, 0.45, 0.48)

GISS-E2-R (0.61, 0.63, 0.50)

HadGEM2-ES (0.47, 0.53, 0.45)

inmcm4 (0.38, 0.36, 0.39)

IPSL-CM5A-LR (0.35, 0.37, 0.40)

IPSL-CM5A-MR (0.42, 0.48, 0.18)

IPSL-CM5B-LR (0.48, 0.49, 0.38)

MIROC5 (0.65, 0.73, 0.36)

MRI-CGCM3 (0.66, 0.75, 0.30)

NorESM1-M (0.38, 0.53, 0.17)

MME-mean (0.64, 0.71, 0.31)

/mm day^{-1}

−2.2 −1.4 −0.6 0.2 1.0 1.8

FIG. 9. As in Fig. 6, but for the abrupt4xCO2 minus piControl January–December mean diagnosed precipitation anomalies.
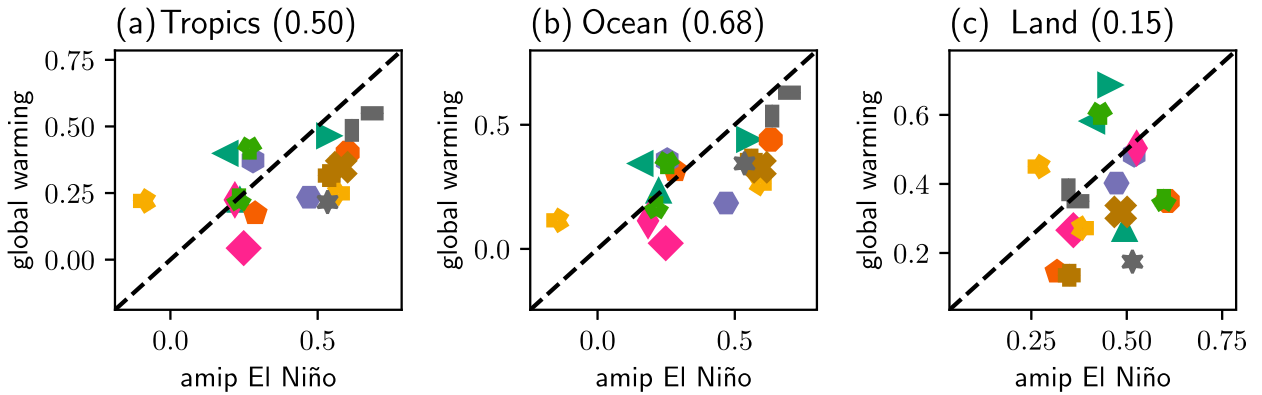
FIG. 10. RH partial 2D diagnosis performance (spatial correlation) for amip El Niño vs abrupt4xCO2 minus piControl global warming for the (a) tropics, (b) tropical ocean, and (c) land grid points. The dashed black line indicates the diagonal, and markers are as in Fig. 8.

MIROC5, and IPSL-CM5A-LR, simulate small-scale, local precipitation changes with large spatial heterogeneity. Subsequently, the diagnosis method fails to detect these weak signals. Regionally, diagnosis performance is quite model dependent. Examining larger-scale simulated precipitation changes over tropical Africa, the correct sign is diagnosed for ACCESS1.3 and BNU-ESM. However, CCSM4, HadGEM2-ES, CanESM2, and NorESM1-M simulate increases in precipitation that are falsely diagnosed as decreases. Diagnosis performance for the MME is stronger over tropical South America, where the simulated precipitation decreases are correctly diagnosed for ACCESS1.0, ACCESS1.3, CanESM2, CCSM4, and NorESM1-M. Diagnosis performance over land is related to the satisfaction of the method assumptions for each model simulation, as discussed in section 5.

Comparing RH partial 2D diagnoses for amip El Niño and global warming precipitation changes, there is a significant correlation in intermodel variability in performance over ocean (0.68). This contributes to a positive correlation in performance across the tropics (0.5),

despite a very weak correlation in performance over land (0.15). In addition, Fig. 10b demonstrates evidence of a linear association between amip El Niño and global warming RH partial 2D performance over ocean. Similarly, the intermodel correlation between piControl El Niño and global warming performance over ocean is larger (0.53) than for performance over land (0.15). Therefore, in models where the RH partial 2D method performs well over ocean at diagnosing El Niño shifts, typically the method also performs well at diagnosing global warming shifts, and vice versa.

Notably, correlations in intermodel variability between the 2D diagnosis method performance for amip El Niño and global warming precipitation changes are weaker across the tropics (0.25) and over tropical ocean (0.40) (Fig. 11). Similar weaker relationships between piControl El Niño performance and global warming performance over the tropics (-0.03) and tropical oceans (0.1) are also present. This suggests that the inclusion of SAT bin number changes affects the method performance differently for El Niño and global warming
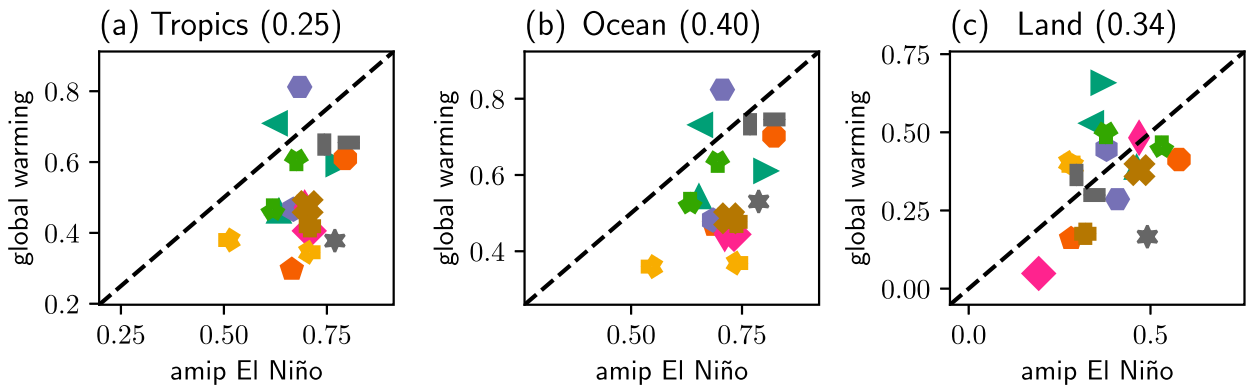

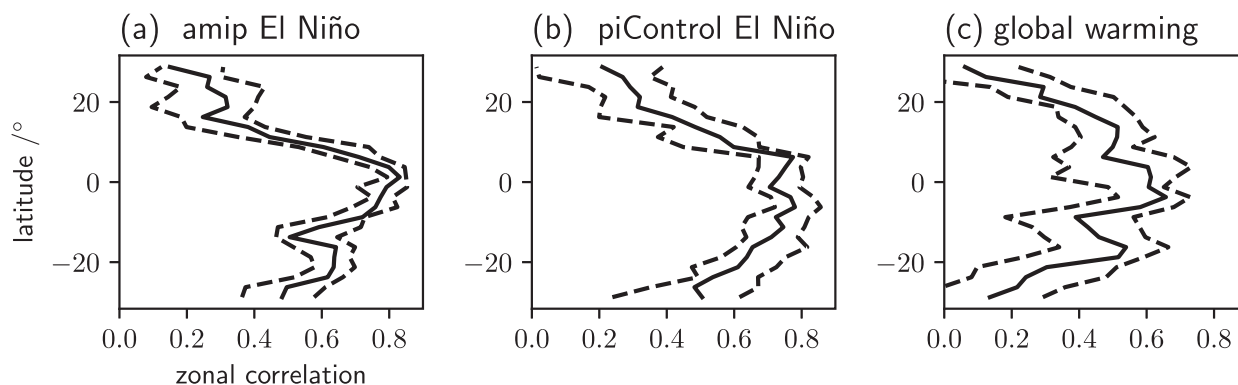FIG. 11. As in Fig. 10, but for 2D diagnosis performance.

FIG. 12. Zonal correlation vs latitude for simulated and diagnosed precipitation anomalies for (a) amip El Niño, (b) piControl El Niño, and (c) abrupt4xCO2 minus piControl global warming. Black lines show the median (solid) and upper and lower quartiles (dashed) of the CMIP5 multimodel ensemble variability.

precipitation changes, mainly over tropical oceans. For amip El Niño diagnoses, the inclusion of SAT bin number changes in the 2D configuration improves weaker performance greatly and stronger performance more weakly. For example, the INM-CM4.0 spatial correlations increase from −0.15 to 0.51, whereas the MRI-CGCM3 spatial correlations increase from 0.65 to 0.8. In contrast, using SAT bin number changes in the 2D configuration improves performance more uniformly for diagnosed global warming precipitation changes. These results indicate that the precipitation–RH bin link over ocean is consistent within models for both El Niño and global warming precipitation changes. The relationship between RH partial 2D and 2D performance in the MME is discussed further in appendix B.

A more consistent result linking El Niño and global warming diagnoses is presented by assessing spatial variations in the performance of the Lambert et al. (2017) method. We define the zonal correlation as the gridpoint correlation between simulated and diagnosed precipitation changes along each 2.5° latitude band. These zonal correlations are calculated for each model in the MME for the amip and piControl El Niño and global warming precipitation changes. The MME median and interquartile range of these zonal correlations for each case are displayed in Fig. 12. The interquartile ranges are relatively narrow, especially for the El Niño cases, suggesting that the MME median is representative of each model. Zonal correlation is largest near the equator for the amip (0.8) and piControl (0.7) El Niño and for the global warming–diagnosed precipitation changes (0.65). In each case, the MME median zonal correlation decreases rapidly poleward. Correspondingly, the magnitude of simulated free-tropospheric temperature gradients is weakest near the equator and increases poleward, similar to ERA-Interim, as discussed in section 4.

Additionally, the link between surface and lower-tropospheric RH is weakest in subtropical regions. This suggests that the Lambert et al. (2017) method performs best in the deep tropics and is weaker in subtropical regions for both El Niño and global warming precipitation changes. Furthermore, this variation in performance is consistently linked in each model with the suitability of the method assumptions.

7. Summary and conclusions

Returning to the introduction, the first question to address is this: Does the Lambert et al. (2017) method adequately diagnose present-day ENSO precipitation shifts? The results presented in sections 4 and 5 demonstrate moderately good performance of the diagnosis method for observations and reanalysis (ERA-Interim–GPCP), and climate model simulations. Furthermore, in ERA-Interim–GPCP, the method performs successfully, as the main assumptions are well justified. Precipitation as a function of local RH and SAT is similar for both El Niño and neutral conditions, supported by Fig. 1a. This is perhaps a necessary result to suggest that precipitation as a function of relative RH and SAT may remain invariant under future climate perturbations. In addition, the disparity in performance over tropical land and ocean may be linked with the applicability of the WTG approximation over these domains. This demonstrates an important factor that influences the performance of the prediction method.

Considering predictions of ENSO simulated precipitation shifts in climate models, performance disparity over land and ocean is a consistent feature with the observations and reanalysis. Overall performance across the tropics is quite good in a variety of model simulations in both atmosphere-only and coupled experiments. This demonstrates that the method is flexible because it

performs well for a variety of simulated El Niño SST patterns. Moreover, there is evidence of a linear relationship (0.64) in performance over ocean between the two experiments. This suggests that the ability of the method to diagnose precipitation shifts over ocean is relatively independent of how SST conditions are simulated. Therefore, model differences in atmospheric processes are a likely source of method performance variability. Analyzing 1D and partial 2D configurations of the Lambert et al. (2017) method, surface RH is a more important predictor than SAT for ENSO precipitation diagnosis. In particular, including SAT changes in the method does not improve the performance over land.

A second question was presented in the introduction: What factors influence the performance of the diagnosis method for ENSO and global warming precipitation shifts? Section 6 presents moderate evidence of a linear relationship (0.68) in prediction performance over ocean between amip ENSO and abrupt4xCO2 minus piControl global warming simulations for the RH partial 2D method. We suggest that this link in performance is associated with a common RH and precipitation change process over ocean for both simulated ENSO and global warming. An interesting question for future work is why SAT affects diagnosis performance differently for ENSO and global warming precipitation changes. A robust relationship between the spatial performance of the diagnosis method and the suitability of the WTG approximation is present for both simulated El Niño and global warming precipitation changes, with the method performing better in the equatorial regions in both cases. Furthermore, method performance weakens as horizontal temperature gradients increase poleward of the deep tropics for both ENSO and global warming.

Linking to Lambert et al. (2017), an important finding of this work is that areas of relatively high RH are observed over land in the present day. Therefore, simulated decreases in RH under global warming could plausibly lead to reduced precipitation via the diagnosis method presented here. In addition, some CMIP5 model piControl simulations have a large negative RH bias over land and, hence, are inconsistent with present-day observations. These models simulate an increase in tropical precipitation over some tropical land areas under global warming, which may be unrealistic due to this RH bias.

A few caveats and important areas of future work are associated with this study. There are large differences in the magnitude of observed ENSO and simulated global warming RH and SAT changes. Performance of the diagnosis method over land for observed El Niño shifts is quite weak (0.46), and there is broad intermodel variability for both amip (0.19–0.58) and piControl

(0.21–0.52) simulations. It is also important to note that the majority of large observed ENSO precipitation changes are over ocean, so the ENSO signal is relatively weaker over tropical land. Additionally, various conflicting factors may contribute to this poor performance over land, as discussed in section 4. One method to quantify the effect of these factors on diagnosis performance would be to use multiple regression; this could form the basis for a future study. Another area of future work is to implement the Lambert et al. (2017) method in an appropriate statistical modeling framework, such as a generalized additive model (Wood 2006), in order to calculate uncertainty estimates for the diagnosed precipitation shifts. This could lead to a more robust assessment of the diagnosis method performance.

The Lambert et al. (2017) diagnosis method postulates that precipitation changes can be characterized by relative changes in SAT and RH. From the results presented in this study, we suggest that the performance of this diagnosis method is related to the satisfaction of three main assumptions: 1) tropical precipitation as a function of SAT and RH bin number is structurally similar under climate perturbations; 2) free-tropospheric horizontal temperature gradients are small, so relative surface conditions influence convection; and 3) surface and lower-tropospheric RH changes are linked. This study and the Lambert et al. (2017) method improve our understanding of the problems surrounding prediction of future precipitation shifts. Markedly different mechanisms contribute to simulated precipitation change for ENSO and global warming. However, a consistent feature across observations, reanalysis, and atmosphere-only and coupled climate model simulations is that the heaviest tropical precipitation is typically anchored above the relatively warmest and most humid locations. We have illustrated how under climate perturbations such as ENSO or global warming, shifts in tropical precipitation can be largely determined by changes in surface relative humidity and air temperature.
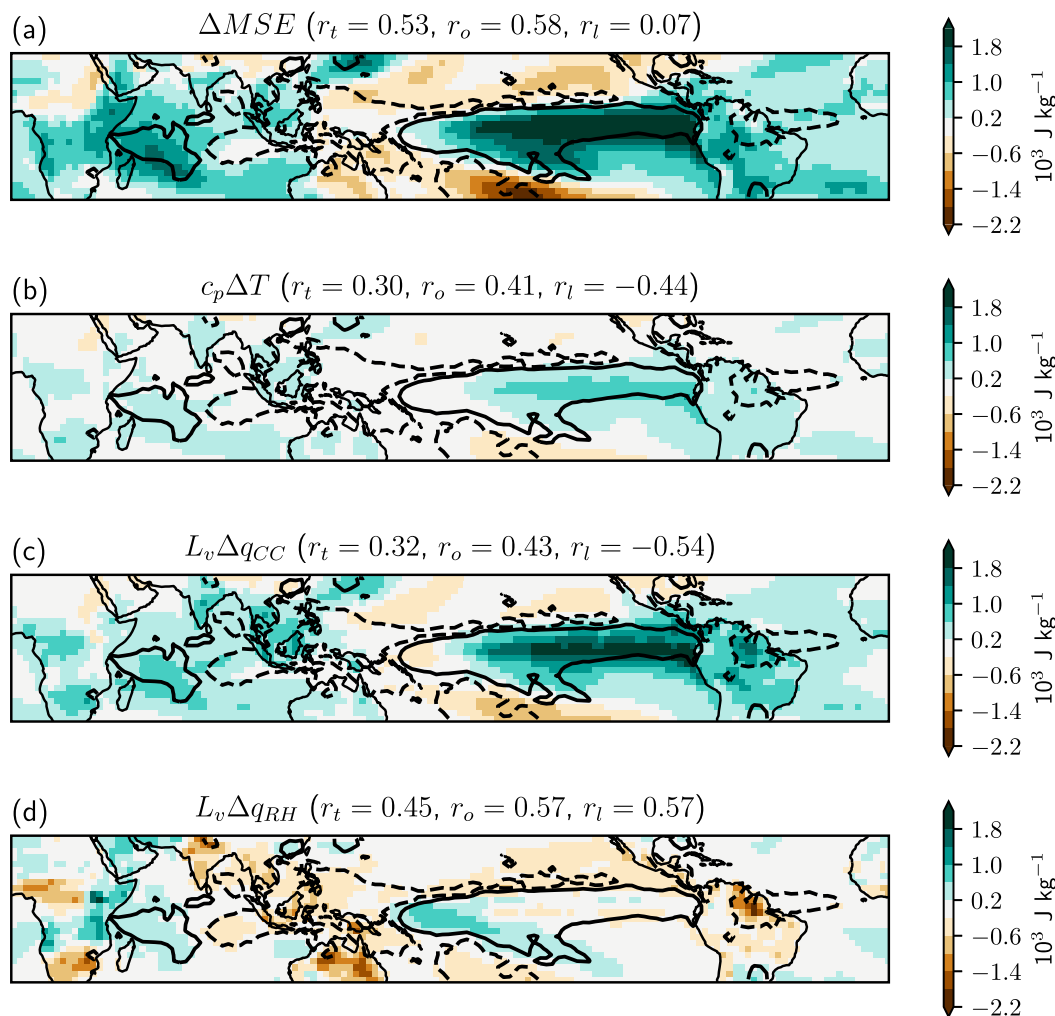
FIG. A1. Color shading shows the July–June El Niño minus neutral mean surface (a) MSE change and its decomposition, (b) MSE changes directly due to temperature changes, (c) MSE changes due to the effect of temperature change on specific humidity change, and (d) MSE changes due to relative humidity changes. Black contours indicate the -0.5 (dashed) and 0.5 (solid) mm day^{-1} GPCP precipitation change, and r_t, r_o, and r_l indicate the spatial correlation with the precipitation change over the tropical, oceanic, and land grid points, respectively.

APPENDIX A

Relative Contributions of RH and SAT to Low-Level MSE

To examine the relative effects of RH and SAT changes to precipitation changes, we decompose low-level moist static energy (MSE) changes. Low-level MSE is defined as $L_v q + c_p T$, where q and T are surface specific humidity and air temperature, respectively, $L_v \approx 2.5 \times 10^6$ J kg^{-1} is the latent heat of vaporization of water, and $c_p \approx 1005$ J kg^{-1} K^{-1} is the specific heat capacity of air at constant pressure. Specific humidity is a function of relative humidity and temperature. A component of specific humidity change linking the Clausius–Clapeyron relation Δq_{CC} is due to a fractional change in saturated vapor pressure with temperature change. The residual component of specific humidity change $\Delta q_{RH} = \Delta q - \Delta q_{CC}$ is therefore linked with relative humidity changes (Chadwick et al. 2013). Changes in low-level MSE can thus be decomposed into
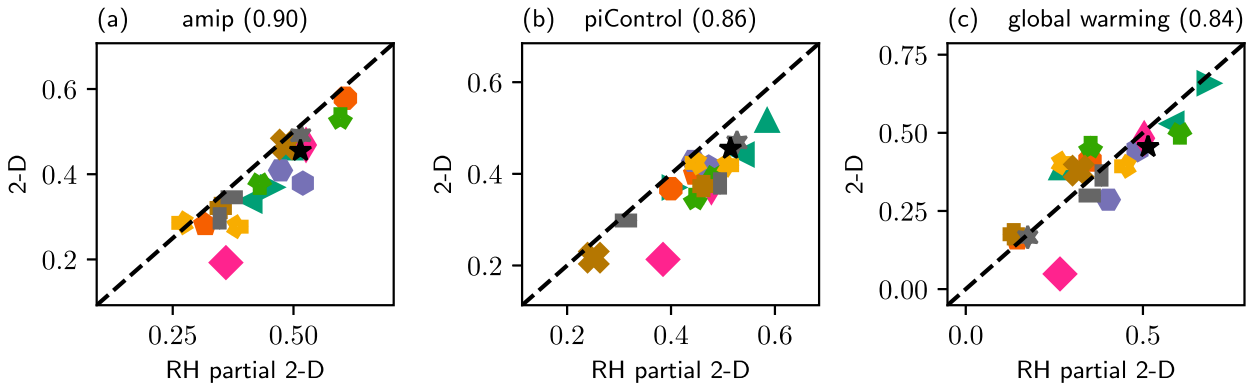
FIG. B1. RH partial 2D vs 2D diagnosis performance (spatial correlation) over land grid points for (a) amip El Niño, (b) piControl El Niño, and (c) abrupt4xCO2 minus piControl. The dashed black line indicates the 1:1 diagonal, markers are as in Fig. 8, and the black star indicates ERA-Interim–GPCP for reference.

three terms: $\Delta\text{MSE} = L_v\Delta q_{\text{RH}} + L_v\Delta q_{\text{CC}} + c_p\Delta T$. Here, $L_v\Delta q_{\text{RH}}$ and $L_v\Delta q_{\text{CC}} + c_p\Delta T$ represent MSE changes associated with RH and SAT changes, respectively.

ERA-Interim El Niño changes in low-level MSE are moderately correlated with GPCP precipitation changes over ocean (0.58) but are uncorrelated over land (0.07), as demonstrated by Fig. A1a. This suggests that different mechanisms may control precipitation changes over land and ocean. The decomposition of the low-level MSE change is shown in Figs. A1b–d. The RH-related component $L_v\Delta q_{\text{RH}}$ is correlated with precipitation changes over both land (0.57) and ocean (0.57). In contrast, the SAT-related components, $c_p\Delta T$ and $L_v\Delta q_{\text{CC}}$, are anticorrelated with precipitation change over land. These results indicate that the dominance of RH changes over SAT changes for diagnosing ENSO precipitation changes is not simply explained by their relative contributions to low-level MSE changes. Other mechanisms, such as changes in lifting condensation level or entrainment, may be important for determining changes in convection.

APPENDIX B

Comparing RH Partial 2D and 2D Configurations of the Lambert et al. (2017) Method

Intermodel variability demonstrates that RH partial 2D and 2D performance over land and ocean is well correlated for amip (0.9 over land, 0.88 over ocean) and piControl (0.86 over land, 0.79 over ocean) El Niño precipitation changes, as well as global warming precipitation changes (0.84 over land, 0.55 over ocean). Additionally, Fig. B1 indicates that RH partial 2D and 2D performance over land is linearly related and approximately equivalent in each model for the three cases. This suggests that including SAT bin number changes in the 2D diagnosis method does not substantially affect performance over land. However, Fig. B2 demonstrates that the 2D configuration consistently outperforms the RH partial 2D configuration over ocean. This highlights the influence of SAT bin number changes in contributing to El Niño and global warming
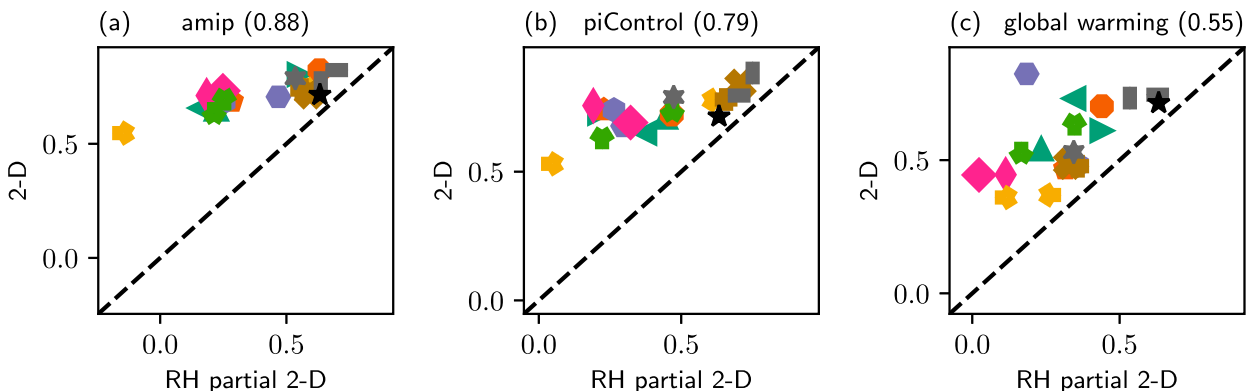

FIG. B2. As in Fig B1, but over ocean grid points.

precipitation changes over ocean. This supports results in the literature suggesting that tropical SST and precipitation pattern changes under global warming are likely to be strongly linked (Xie et al. 2010).

REFERENCES

Adler, R. F., and Coauthors, 2003: The Version-2 Global Precipitation Climatology Project (GPCP) monthly precipitation analysis (1979–present). *J. Hydrometeor.*, **4**, 1147–1167, https://doi.org/10.1175/1525-7541(2003)004<1147:TVGPCP>2.0.CO;2.

Bellenger, H., E. Guilyardi, J. Leloup, M. Lengaigne, and J. Vialard, 2014: ENSO representation in climate models: From CMIP3 to CMIP5. *Climate Dyn.*, **42**, 1999–2018, https://doi.org/10.1007/s00382-013-1783-z.

Bretherton, C. S., and A. H. Sobel, 2002: A simple model of a convectively coupled Walker circulation using the weak temperature gradient approximation. *J. Climate*, **15**, 2907–2920, https://doi.org/10.1175/1520-0442(2002)015<2907:ASMOAC>2.0.CO;2.

——, and ——, 2003: The Gill model and the weak temperature gradient approximation. *J. Atmos. Sci.*, **60**, 451–460, https://doi.org/10.1175/1520-0469(2003)060<0451:TGMATW>2.0.CO;2.

——, M. E. Peters, and L. E. Back, 2004: Relationships between water vapor path and precipitation over the tropical oceans. *J. Climate*, **17**, 1517–1528, https://doi.org/10.1175/1520-0442(2004)017<1517:RBWVPA>2.0.CO;2.

Byrne, M. P., and P. A. O'Gorman, 2016: Understanding decreases in land relative humidity with global warming: Conceptual model and GCM simulations. *J. Climate*, **29**, 9045–9061, https://doi.org/10.1175/JCLI-D-16-0351.1.

——, and T. Schneider, 2016: Narrowing of the ITCZ in a warming climate: Physical mechanisms. *Geophys. Res. Lett.*, **43**, 11 350–11 357, https://doi.org/10.1002/2016GL070396.

Chadwick, R., I. Boutle, and G. Martin, 2013: Spatial patterns of precipitation change in CMIP5: Why the rich do not get richer in the tropics. *J. Climate*, **26**, 3803–3822, https://doi.org/10.1175/JCLI-D-12-00543.1.

——, P. Good, and K. Willett, 2016: A simple moisture advection model of specific humidity change over land in response to SST warming. *J. Climate*, **29**, 7613–7632, https://doi.org/10.1175/JCLI-D-16-0241.1.

——, H. Douville, and C. B. Skinner, 2017: Timeslice experiments for understanding regional climate projections: Applications to the tropical hydrological cycle and European winter circulation. *Climate Dyn.*, **49**, 3011–3029, https://doi.org/10.1007/s00382-016-3488-6.

Charney, J. G., 1963: A note on large-scale motions in the tropics. *J. Atmos. Sci.*, **20**, 607–609, https://doi.org/10.1175/1520-0469(1963)020<0607:ANOLSM>2.0.CO;2.

Christensen, J. H., and Coauthors, 2013: Climate change phenomena and their relevance for future regional climate change. *Climate Change 2013: The Physical Science Basis*, T. F. Stocker et al., Eds., Cambridge University Press, 1217–1308.

Collins, M., and Coauthors, 2013: Long-term climate change: Projections, commitments and irreversibility. *Climate Change 2013: The Physical Science Basis*, T. F. Stocker et al., Eds., 1029–1136.

Cowtan, K., and R. G. Way, 2014: Coverage bias in the HadCRUT4 temperature series and its impact on recent temperature trends. *Quart. J. Roy. Meteor. Soc.*, **140**, 1935–1944, https://doi.org/10.1002/qj.2297.

Dee, D. P., and Coauthors, 2011: The ERA-Interim reanalysis: Configuration and performance of the data assimilation system. *Quart. J. Roy. Meteor. Soc.*, **137**, 553–597, https://doi.org/10.1002/qj.828.

ECMWF, 2016: IFS documentation—Cy43r1 operational implementation 22 Nov 2016—Part IV: Physical processes. ECMWF Rep., 223 pp., https://www.ecmwf.int/sites/default/files/elibrary/2016/17117-part-iv-physical-processes.pdf.

Flato, G., and Coauthors, 2013: Evaluation of climate models. *Climate Change 2013: The Physical Science Basis*, T. F. Stocker et al., Eds., Cambridge University Press, 741–866.

Guilyardi, E., A. Wittenberg, A. Fedorov, M. Collins, C. Wang, A. Capotondi, G. J. van Oldenborgh, and T. Stockdale, 2009: Understanding El Niño in ocean–atmosphere general circulation models: Progress and challenges. *Bull. Amer. Meteor. Soc.*, **90**, 325–340, https://doi.org/10.1175/2008BAMS2387.1.

Held, I. M., and B. J. Soden, 2006: Robust responses of the hydrological cycle to global warming. *J. Climate*, **19**, 5686–5699, https://doi.org/10.1175/JCLI3990.1; Corrigendum, **24**, 1559–1560, https://doi.org/10.1175/2010JCLI4045.1.

Holloway, C. E., and J. D. Neelin, 2009: Moisture vertical structure, column water vapor, and tropical deep convection. *J. Atmos. Sci.*, **66**, 1665–1683, https://doi.org/10.1175/2008JAS2806.1.

Jolliffe, I. T., and D. B. Stephenson, 2012: *Forecast Verification: A Practitioner's Guide in Atmospheric Science*. John Wiley & Sons, 274 pp.

Knutti, R., and J. Sedláček, 2013: Robustness and uncertainties in the new CMIP5 climate model projections. *Nat. Climate Change*, **3**, 369–373, https://doi.org/10.1038/nclimate1716.

Kuo, Y.-H., J. D. Neelin, and C. R. Mechoso, 2017: Tropical convective transition statistics and causality in the water vapor–precipitation relation. *J. Atmos. Sci.*, **74**, 915–931, https://doi.org/10.1175/JAS-D-16-0182.1.

Lambert, F. H., A. J. Ferraro, and R. Chadwick, 2017: Land–ocean shifts in tropical precipitation linked to surface temperature and humidity change. *J. Climate*, **30**, 4527–4545, https://doi.org/10.1175/JCLI-D-16-0649.1.

Lau, W. K. M., and K.-M. Kim, 2015: Robust Hadley circulation changes and increasing global dryness due to CO_2 warming from CMIP5 model projections. *Proc. Natl. Acad. Sci. USA*, **112**, 3630–3635, https://doi.org/10.1073/pnas.1418682112.

McPhaden, M. J., S. E. Zebiak, and M. H. Glantz, 2006: ENSO as an integrating concept in Earth science. *Science*, **314**, 1740–1745, https://doi.org/10.1126/science.1132588.

Neelin, J. D., D. S. Battisti, A. C. Hirst, F.-F. Jin, Y. Wakata, T. Yamagata, and S. E. Zebiak, 1998: ENSO theory. *J. Geophys. Res.*, **103**, 14 261–14 290, https://doi.org/10.1029/97JC03424.

Nesbitt, S. W., and E. J. Zipser, 2003: The diurnal cycle of rainfall and convective intensity according to three years of TRMM measurements. *J. Climate*, **16**, 1456–1475, https://doi.org/10.1175/1520-0442-16.10.1456.

NOAA, 2015: Historical El Niño/La Niña episodes (1950–present). National Weather Service Climate Prediction Center, accessed 13 January 2017, http://www.cpc.ncep.noaa.gov/products/analysis_monitoring/ensostuff/ensoyears.shtml.

Pfhal, S., and N. Niedermann, 2011: Daily covariations in near-surface relative humidity and temperature over the ocean. *J. Geophys. Res.*, **116**, D19104, https://doi.org/10.1029/2011JD015792.

Ropelewski, C. F., and M. S. Halpert, 1987: Global and regional scale precipitation patterns associated with the El Niño/Southern Oscillation. *Mon. Wea. Rev.*, **115**, 1606–1626, https://doi.org/10.1175/1520-0493(1987)115<1606:GARSPP>2.0.CO;2.

Rosenfeld, D., U. Lohmann, G. B. Raga, C. D. O'Dowd, M. Kulmala, S. Fuzzi, A. Reissell, and M. O. Andreae, 2008:

Flood or drought: How do aerosols affect precipitation? *Science*, **321**, 1309–1313, https://doi.org/10.1126/science.1160606.

Schiro, K. A., J. D. Neelin, D. K. Adams, and B. R. Lintner, 2016: Deep convection and column water vapor over tropical land versus tropical ocean: A comparison between the Amazon and the tropical western Pacific. *J. Atmos. Sci.*, **73**, 4043–4063, https://doi.org/10.1175/JAS-D-16-0119.1.

Seager, R., N. Naik, and G. A. Vecchi, 2010: Thermodynamic and dynamic mechanisms for large-scale changes in the hydrological cycle in response to global warming. *J. Climate*, **23**, 4651–4668, https://doi.org/10.1175/2010JCLI3655.1.

Seidel, D. J., Q. Fu, W. J. Randel, and T. J. Reichler, 2008: Widening of the tropical belt in a changing climate. *Nat. Geosci.*, **1**, 21–24, https://doi.org/10.1038/ngeo.2007.38.

Sherwood, S. C., R. Roca, T. M. Weckwerth, and N. G. Andronova, 2010: Tropospheric water vapor, convection, and climate. *Rev. Geophys.*, **48**, RG2001, https://doi.org/10.1029/2009RG000301.

Sobel, A. H., and C. S. Bretherton, 2000: Modeling tropical precipitation in a single column. *J. Climate*, **13**, 4378–4392, https://doi.org/10.1175/1520-0442(2000)013<4378:MTPIAS>2.0.CO;2.

——, J. Nilsson, and L. M. Polvani, 2001: The weak temperature gradient approximation and balanced tropical moisture waves. *J. Atmos. Sci.*, **58**, 3650–3665, https://doi.org/10.1175/1520-0469(2001)058<3650:TWTGAA>2.0.CO;2.

Taylor, K. E., R. J. Stouffer, and G. A. Meehl, 2012: An overview of CMIP5 and the experiment design. *Bull. Amer. Meteor. Soc.*, **93**, 485–498, https://doi.org/10.1175/BAMS-D-11-00094.1.

Trenberth, K. E., and D. P. Stepaniak, 2001: Indices of El Niño evolution. *J. Climate*, **14**, 1697–1701, https://doi.org/10.1175/1520-0442(2001)014<1697:LIOENO>2.0.CO;2.

Vecchi, G. A., and B. J. Soden, 2007: Global warming and the weakening of the tropical circulation. *J. Climate*, **20**, 4316–4340, https://doi.org/10.1175/JCLI4258.1.

Wood, S. N., 2006: *Generalized Additive Models: An Introduction with R*. Chapman & Hall/CRC, 410 pp.

Xie, S.-P., C. Deser, G. A. Vecchi, J. Ma, H. Teng, and A. T. Wittenberg, 2010: Global warming pattern formation: Sea surface temperature and rainfall. *J. Climate*, **23**, 966–986, https://doi.org/10.1175/2009JCLI3329.1.